Imaging artificial salt water infiltration using electrical resistivity tomography constrained by geostatistical data

Hermans T.[1], Vandenbohede A.[2], Lebbe L. [2], Martin R.[3], Kemna A. [3], Beaujean J.[4] and Nguyen F. [4]

Published in *Journal of Hydrology*:

http://www.sciencedirect.com/science/journal/00221694

http://www.journals.elsevier.com/journal-of-hydrology/

Please cite as:

Hermans T., Vandenbohede A., Lebbe L., Martin R., Kemna A., Beaujean J. and Nguyen F. 2012. Imaging artificial salt water infiltration using electrical resistivity tomography constrained by geostatistical data, Journal of Hydrology, 438-439, 168-180.

http://dx.doi.org/10.1016/j.jhydrol.2012.03.021

[1]Aspirant F.R.S-FNRS, ArGEnCo – GEO³, Applied Geophysics, Liege University, Chemin des Chevreuils, 1, B-4000 Liege, Belgium, thomas.hermans@ulg.ac.be.

[2]Research Unit Groundwater Modelling, Dept. Geology and Soil Science, Ghent University Krijgslaan 281 (S8), B-9000 Gent, Belgium.

alexander.vandenbohede@ugent.be, luc.lebbe@ugent.be.

[3]Department of Geodynamics and Geophysics, Steinmann Institute, University of Bonn, Meckenheimer Allee 176, D-53115, Bonn, Germany. rmartin@geo.uni-bonn.de, kemna@geo.uni-bonn.de.

[4]ArGEnCo – GEO³, Applied Geophysics, Liege University, Chemin des Chevreuils, 1, B-4000 Liege, Belgium. jean.beaujean@ulg.ac.be, f.nguyen@ulg.ac.be.

Abstract

Electrical resistivity tomography is a well-known technique to monitor fresh-salt water transitions. In such environments, boreholes are often used to validate geophysical results but rarely used to constrain the geoelectrical inversion. To estimate the extent of salt water infiltration in the dune area of a Natural Reserve (Westhoek, Belgium), electrical resistivity tomography profiles were carried out together with borehole electromagnetic measurements. The latter were used to calculate a vertical variogram, representative of the study site. Then, a geostatistical constraint, in the form of an *a priori* model covariance matrix based on the variogram, was imposed as regularization to solve the electrical inverse problem. Inversion results enabled to determine the extension of the salt water plume laterally and at depth, but also to estimate the total dissolved solid content within the plume. These results are in agreement with the hydrogeological data of the site. A comparison with borehole data showed that the inversion results with geostatistical constraints are much more representative of the seawater body (in terms of total dissolved solids, extension and height) than results using standard smoothness-constrained inversion. The field results obtained for the Westhoek site emphasize the need to go beyond standard smoothness-constrained images and to use available borehole data as prior information to constrain the inversion.

Keywords: salt water intrusion, electrical resistivity tomography, geostatistical constraint, variogram, inversion, regularization.

1. Introduction

Sea water intrusion problems concern many countries around the world since coastal areas provide inhabitants with places very well situated for economic development and life quality. In the future, the amount of people living in coastal areas is expected to grow strongly, increasing the human pressure on hydrogeological equilibriums (The Earth Institute Columbia University, 2006). To manage efficiently coastal areas and salt/fresh water distributions, reliable measurements and robust interpretation methods are necessary.

In the context of this work, we investigate the Flemish Nature Reserve "The Westhoek" situated along the French-Belgian border in the western Belgian coastal plain (FIG. 1A). In this reserve, two artificial sea inlets were made in the fore dunes. Sea water has thereby access to two hinter lying dune slacks. However, a fresh water lens is present in the dune aquifer, which is exploited for production of drinking water (FIG. 1A, water catchment). It is thus very important to know the spatial extent of the body of infiltrated salt water.

In last years, several geophysical studies were conducted in the context of saltwater intrusions (e.g. Carter et al., 2008; De Franco et al., 2009; Goldman and Kafri, 2006 and references therein; Martinez et al., 2009; Nguyen et al., 2009). Among the different geophysical methods, the ability of electrical resistivity tomography (ERT) to detect and monitor fresh-salt water transitions in different coastal areas was proven efficient and rapidly gained popularity among scientists (e.g. Nguyen et al., 2009).

Most of the studies use geophysical data as qualitative information although quantitative estimates of physical properties of interest may be retrieved in a quantitative way. For example, Goldman and Kafri (2006) described a methodology to calculate porosity from time-domain electromagnetic data and electrical measurements, based on Archie's law (Archie, 1942). Amidu and Dunbar (2008) evaluated the potential of electrical resistivity inversion methods for water-reservoir salinity studies. They optimized inversion parameters

(regularization or damping factor) using realistic synthetic cases and imposed electrical conductivity values to constrain the inversion where such measurements were available. Nguyen et al. (2009) proposed a methodology to analyze ERT images in order to assess where resolution (based on cumulative sensitivity) is sufficient to be used for hydrogeological model calibration according to the correlation between targeted and imaged salt mass fraction values.

These different studies highlight the fact that borehole data are often necessary to interpret inversion results more accurately, to convert resistivity into salinity or to assess the quality of inversion results. However, few studies (e.g. Amidu and Dunbar, 2008 ; Nguyen et al., 2009) have used borehole data as additional constraints in the inversion process. In ERT, the inversion is usually limited to standard smoothness-constraint regularization (Constable et al., 1987; deGroot-Hedlin and Constable, 1990; Smith and Booker, 1988).

In this study, we use electromagnetic induction (EM39, Geonics© (McNeill, 1986)) borehole logging data to constrain the vertical correlation length of sediment bulk electrical conductivity within geostatistical regularization of 2D-surface ERT. This is performed by incorporating *a priori* information in the inversion in the form of a model covariance matrix (Martin et al., 2010).

This technique is a least squares approach and differs from geostatistical inverse modeling which is a probabilistic approach aiming at determining the most likely estimates. Within this context, nonlinear problems are solved using an iterative inversion scheme solving the co-kriging equations. We refer to Yeh et al. (1996) for more details about this inversion approach and to Yeh et al. (2002, 2006) for applications to ERT.

The theoretical concept to use statistical information within geophysical inverse solutions by utilizing *a priori* model covariance matrices is based on the work of Tarantola and Valette (1982), who showed the application and estimation of a Gaussian covariance model to invert 1D synthetic gravity data. Pilkington and Todoeschuk (1991) used well log data to apply this

concept within 1D magnetotelluric and DC resistivity inversions. Maurer et al. (1998) used a general model utilizing the von Kármán autocovariance function to regularize large-scale geophysical inverse problems, namely to invert 2D cross-borehole seismic data. They also showed the similarity between the so-called stochastic regularization operator, the damping and the smooth-model regularization operator. Yang and LaBrecque (1998) parameterized covariance functions, which are well known geostatistical tools frequently used within cokriging of geostatistical reservoir modeling (see for instance Journel and Huijbregts, 1978, and Isaaks and Srivastava, 1989), to use as *a priori* covariance within 3D ERT inverse solutions.

Chasseriau and Chouteau (2003) demonstrated the benefits of using *a priori* information in the form of a covariance matrix whose parameters were derived from experimental semivariogram data and used it as regularization operator within reconstruction of large-scale 3D density models. They used the methodology in synthetic benchmark studies and applied the same procedure to field data (scale of several kilometers). More than 3000 gravity measurements were used for horizontal variography, and two boreholes provided vertical information for separate covariogram function calculation.

Linde et al. (2006), extending the work of Maurer et al. (1998), included variogram information to achieve geostatistical regularization for ERT and GPR joint inversion. They exploited linear equidistant grids and utilized a 3D fast Fourier transform for their covariance matrix computation. They demonstrated that this type of regularization preserves spatial statistics of the joint ERT and GPR images in comparison to classical smooth-model solutions. Yet, their method is only applicable if the grid parameterization is uniform in each spatial direction and thus not applicable for more general model problem geometries, like for the problem considered herein due to topography issues.

Johnson et al. (2007) explored an inversion method to fit high-resolution GPR cross-borehole data and honor experimental variograms simultaneously. They explicitly incorporated a variogram operator in the inversion process (the *a priori* model characteristic is the variogram itself). In this way, they obtained a model fitting both data and statistical parameters. The approach requires calculating the experimental variogram sensitivities in order to modify the model parameters (dielectric permittivities) during the inversion to preserve the spatial statistics. The question of balancing between variogram and data is addressed through additional user-defined criteria. With their method, it is always possible to find a solution reproducing the variograms corresponding to any field (even non-stationary) so long as it also honors the data. They applied this technique to cross-borehole GPR traveltime data and given variograms well constrained in the vertical direction, thanks to available logging data. There remained uncertainty on the horizontal range because of relatively low horizontal sampling.

In this study, we propose a methodology to account for some *a priori* geostatistical information from borehole measurements within our geophysical procedure following the approach of Yang and LaBrecque (1998) and demonstrate the benefits of the method for a field study case at a relevant hydrogeological scale. The paper is organized as follows. First, the geology and hydrogeology of the study site are described. Then, the methodology followed in this study is explained, including variogram computation, ERT inversion procedure and image appraisal tools. After outlining the data acquisition and analysis processes, the results are presented and the paper ends with discussions and conclusions.

2. Geology and hydrogeology of the study site

The Flemish Nature Reserve “The Westhoek” is situated along the French-Belgian border in the western Belgian coastal plain (FIG. 1A). In this reserve, two artificial sea inlets were made in the fore dunes in 2004. Sea water has thereby access to dune slacks. The aim of the

sea inlets is to promote biodiversity and, in particular, to develop natural habitats. Such sea inlets remain a rare phenomenon along the southern North Sea, and they display specialized bird species and also a particular salt tolerant flora (Verwaest et al., 2005). Since the dune slacks are elevated at 5-5.5 mTAW[1] whereas high sea levels can reach 5.6 mTAW, sea water entered the dune slacks during high tide and formed two infiltration ponds. However, a fresh water lens is present in the dune aquifer, which is for instance exploited for production of drinking water (FIG. 1A, water catchment). It is thus very important to know the spatial extent of the body of infiltrated salt water. Indeed, this additional recharge of salt water might modify the hydrological equilibrium (FIG. 2) of the fresh water lens and salt water could threaten the pumping area. A complete description of the site can be found in Vandenbohede et al. (2008).

The dune area consists of Quaternary sand deposits with a thickness of about 30 m (Lebbe, 1978). The lower part consists of medium to coarse medium sands with shells and shells debris of Eemian age. The upper part is constituted by fine to fine-medium sands of Holocene age, with intercalations of clay layers (Lebbe, 1978). This Quaternary phreatic aquifer is bounded below by the clay of the formation of Kortrijk (Eocene), which is about 100 m thick. This formation can be considered as impermeable from a hydrogeological point of view (Vandenbohede et al., 2008).

Two semi-permeable layers with high clay content are present in the phreatic dune aquifer (Lebbe, 1978). One of these is situated directly under the infiltration ponds (FIG. 2). This semi-permeable layer is important since it hinders the downward flow of salt infiltration water and results in a lateral spread of it. Mapping the distribution of salt water (depth and lateral

[1] mTAW (Tweede Algemene Waterpassing), the Belgian reference level, is 2.3m below the mean sea level.

extension) within the fresh water lens using ERT profiles (FIG. 1B) is the main objective of our studies.

The hydrogeological situation (FIG. 2) results from the geological development during the Holocene. From the 7th century AD, the current dune belt started to form and this hampered the sea to enter the hinterland. This situation led to the development of a fresh water lens in the dune area. The dunes have a higher elevation than the sea and the polders, from which water is artificially drained. Part of the fresh water from the dunes flows towards the polder and discharges along the dune-polder boundary. The other part flows towards the sea. This forms a flow of fresh water whose discharge area is along the low water line. Above this fresh water tongue, a salt water lens is present originating from the recharge of salt water on the back shore, mainly during high tide. This salt water flows towards the fore shore where it discharges, mainly during low tides (Lebbe, 1999; Vandenbohede and Lebbe, 2006).

Since 1967, freshwater has been extracted from the dune aquifer to produce drinking water. With the current extraction rate, influence of the water extraction on the study area around the inlets is, however, minimal. Two hydrogeological water divides (see FIG. 2) exist among the dunes: the first one is located more or less in the center of the dunes; the second one is situated to the south of the water extraction zone. The less permeable layers within the Quaternary deposits led to secondary hydrogeological water divides (Vandenbohede et al., 2008).

Seawater infiltrated the dune slacks from the latter part of 2004. From the latter part of 2005, entrance of sea water in the western dune slack was becoming difficult due to silting up of the inlet. Although sand was removed from the inlets several times since then, silting up remains an issue. Therefore, periods of salt water infiltration in the dune slacks themselves occur only sporadically, during periods of high water.

A first monitoring campaign carried out with an electromagnetic induction tool (EM39, Geonics© (McNeill, 1986)) began in 2004 and ended in 2006. The results are described in details in Vandenbohede et al. (2008). This campaign revealed an important horizontal flow component due to the presence of the semi-permeable layer under the infiltration ponds. Because of the lower hydraulic conductivity, downward movement of salt water is hindered. In addition, the local water divide above the high clay horizon moved inland, leading to a potential risk for the water extraction. Further monitoring was thus recommended and electrical resistivity tomography measurements were carried out to improve the knowledge concerning the position of salt water.

During the ERT campaign (see section 3), exploration focused on the smaller eastern pond, because the situation in this pond was potentially worse (higher horizontal flow). In this pond, 5 wells were available to obtain vertical information on the bulk conductivity distribution. This data was used to generate a geostatistical constraint for the ERT inversion.

3. Data acquisition and analysis

3.1. EM39 survey

A new EM39 measurement campaign was carried out in the five still accessible boreholes of the site (P11, P12, P14, P16 and P18 in FIG. 1B) to monitor the evolution of salt water and to provide borehole data to constrain electrical resistivity tomography. The volume investigated by this method is much smaller (the vertical sensitivity is about 50cm and the lateral sensitivity about 1m (McNeill, 1986)) than the one investigated by one ERT data point, leading to a more accurate description of the vertical conductivity distribution. However, the volume investigated by one EM39 measurement is not that different of the one of one cell of the inversion grid, we thus assume that the vertical variogram can be used to constrain the ERT inversion. FIG. 3A gives an example of the evolution of EM39 data (well P11, see FIG. 1B for location) since 2005. Two zones display higher electrical conductivity values. The first

one, around 2.5 mTAW is due to salt water that has sunk deeper down the aquifer after 2005. The small remaining anomaly visible from the 2010 measurements is due to the occurrence of a small shallow clay layer (Lebbe, 1978). The second zone is located around –7 mTAW, i.e. the position of the semi-permeable layer with high clay content (FIG. 3B). Since this layer acts as a barrier to vertical flow, salt water is present, leading to an increase in electrical conductivity, which can be identified from FIG. 3A. However, this anomaly reached its maximum in 2009, but the maximum value decreased by about 30% in 2010, certainly because of groundwater movement. Between these two last measurements, no new intrusion likely occurred at the location of this well because of the silting up of the inlets.

3.2. Electrical resistivity campaign

3.2.1. Acquisition

The electrical resistivity campaign was carried out in order to detect the salt water depth and its lateral extension. Data sets were collected for six 2D profiles. Three profiles were placed parallel to the coast line (profile numbers 1, 4 and 6) and three other perpendicular to it (profile numbers 2, 3 and 5) in order to cover the whole pond area. The positions of wells and profiles are shown in FIG. 1B.

A dipole-dipole electrode array (dipole length up to its maximum value, dipole separation factor *n* equal or lower than 6) was chosen because of its resolution (Dahlin and Zhou, 2004). With this configuration, an electrode spacing of 3m was chosen to reach the targeted depth of investigation (about 20-30 m according to the thicknesses of the Quaternary deposits) which is related to the maximum offset. We used a Syscal Pro resistivity-meter (10 recording channels) to collect the resistance data. For profiles 1, 2, 4 and 6 we used 72 electrodes (1078 measurements) whereas for profiles 3 and 5 we used 48 electrodes (629 measurements).

3.2.2. Data error analysis

The estimation of data error is a very important issue in ERT (e.g. LaBrecque et al., 1996). An overestimation of the noise level leads to over-smoothed images. In contrast, when the error is underestimated, the inversion algorithm will try to achieve this level by generating artifacts, typically reflected as rough and irregular structures, which can easily lead to misinterpretations.

To estimate the data error, reciprocal resistance measurements were collected for each profile. Reciprocal measurements are obtained by swapping current and potential dipoles. This should not change the value of resistance in linear heterogeneous media (Parasnis, 1988). In contrast with repeatability measurements, some factors are changed when potential and injection dipoles are swapped for reciprocal measurements. This reduces the amount of systematic error (even if it does not eliminate all of them) and can further be used to assess the error level in the data (LaBrecque et al., 1996).

The reciprocal error is defined as

$$e_{N/R} = R_N - R_R, \qquad (1)$$

where R_N and R_R are the normal and reciprocal resistance values, respectively. Slater et al. (2000) propose an error model where this error increases linearly with the mean R of normal and reciprocal resistances:

$$\left|e_{N/R}\right| = a + bR, \qquad (2)$$

where a represents the minimum absolute error and b defines the relative increase of the error with resistance. These parameters are determined by the envelope in an error versus resistance plot that contains all the points after removal of outliers. This is illustrated in FIG. 4 for the entire ERT data set. The best fit for the envelope was found for a = 0.05 Ω and b = 5 %. However, the individual error estimates (Eq. 1) was used in the inversion process, since it was available for each data point (see section 4.2). The error model of Eq. (2) was used to weight a few points for which reciprocal measurements were not available.

4. Methodology

4.1. Geostatistical variogram analysis

In geostatistics, spatial parameters are considered as realization of random variables where one often has to assume stationarity in order to estimate these parameters. This hypothesis assumes that univariate and bivariate (and higher order) statistics are independent from the location *x* (Isaaks and Srivastava, 1989).

For a stationary process, the covariance function $C(h)$ and the variogram $\gamma(h)$, h being the lag, are known to be equivalent

$$\gamma(h) = C(0) - C(h). \quad (3)$$

It is not possible to demonstrate the stationarity of a field, since we only have access to one realization of the random function at any sampling location. In our case, the experimental vertical variogram was calculated for all the electromagnetic conductivity data, transformed in logarithmic value (logarithm of conductivity is the parameter we invert for in the ERT inversion). The model best fitting the borehole data considering the five boreholes together is a Gaussian model

$$\gamma(h) = C(0)(1 - e^{-3(\frac{h}{a})^2}). \quad (4)$$

Its sill $C(0)$ was set equal to the variance (0.37) of the borehole data and the range a was chosen equal to 8.4 m in order to minimize the residue (FIG. 5). The cyclicity observed for the experimental variogram is likely related to the expected layered structure of the clay and sea water infiltration in the subsurface. We do not expect many effects in the results neglecting this hole effect, since it is limited to less than 20% of the variance.

Estimating the horizontal range is a difficult task since we do not have enough data to do it. However, we have to provide an estimate for the inversion. Even if tomograms are of limited help to derive geostatistical parameters, mainly due to variable resolution (Day-Lewis

and Lane, 2004), we used our ERT data to derive an anisotropy ratio between vertical and horizontal ranges. We carried out ERT inversions with isotropic smoothness constraint to have a solution equally smoothed in both directions. Giving this, vertical and horizontal ranges were calculated on the inverted parameters and an anisotropy factor (horizontal over vertical range) of 4 was found. It was decided to keep this anisotropy factor to determine the horizontal range for our geostatistical inversion. Since the vertical range deduced from boreholes is equal to 8.4 m, we derived a horizontal range of 33.6 m.

Once the two main ranges are known, it is possible to calculate the range in any spatial direction where horizontal and vertical axes are considered as ellipsoid axes (Chasseriau and Chouteau, 2003). The generalized range a_α in the direction α (angle between the horizontal axis and the line connecting the concerned grid cells) is equal to

$$a_\alpha = \frac{a_x a_z}{(a_z^2 \cos^2 \alpha + a_x^2 \sin^2 \alpha)^{1/2}} . \qquad (5)$$

The value of the variogram between two parameters is simply determined using equation 4, with $a = a_\alpha$ calculated from equation 5.

4.2. Inversion with geostatistical constraints

For the ERT inverse problem, there is not a unique model that can explain the data. A common way to find a physically plausible solution is to regularize the problem with additional constraint (Tikhonov and Arsenin, 1977) by minimizing an objective function of the form

$$\psi(\mathbf{m}) = \psi_{\mathrm{d}}(\mathbf{m}) + \lambda \psi_{\mathrm{m}}(\mathbf{m}) . \qquad (6)$$

The first term on the right-hand side in equation 6 expresses the data misfit and the second an *a priori* model characteristic. The regularization parameter, λ, balances between these two terms.

Traditional regularization of non-linear electrical and electromagnetic inverse problems utilizes the first-order roughness matrix as regularization operator (Constable et al., 1987), and the *a priori* characteristic of the model is to be smooth.

In our study, an approach similar to the one of Yang and LaBrecque (1998) and Chasseriau and Chouteau (2003) was used. The *a priori* model covariance matrix, $\mathbf{C_m}$, is calculated using equations 3 to 5, and the objective function (equation 6) becomes (Martin et al., 2010)

$$\psi(\mathbf{m}) = \left\|\mathbf{W_d}(\mathbf{d}-\mathbf{f}(\mathbf{m}))\right\|^2 + \lambda\left\|\mathbf{C_m}^{-0.5}(\mathbf{m}-\mathbf{m_0})\right\|^2, \qquad (7)$$

where $\mathbf{W_d}$ is a diagonal matrix (section 3.2.2.), whose entries are the inverse of equation 1, this data error level, as estimated from the reciprocal measurements, was used to weight the data during the inversion; $\mathbf{f}(\mathbf{m})$ is the non-linear operator mapping the model parameters $\mathbf{m}$ (log conductivity) to the data set $\mathbf{d}$ (log resistance), $\mathbf{m_0}$ is a prior model reflecting *a priori* information. The role of the regularization parameter λ is the same than in equation 6. In this paper, we identify the regularization parameter to be proportional to the sill.

The solution of the inverse problem is based on the minimization of the objective function of equation 7 (Kemna, 2000). The problem being non-linear, it is linearized through Taylor expansion around the starting model and solved iteratively utilizing a Gauss-Newton scheme. The iterative process starts with a model $\mathbf{m_0}$, and the minimization of equation 7 provides a model update $\Delta\mathbf{m}_q$ (Kemna, 2000)

$$\mathbf{B}_q\Delta\mathbf{m}_q = \mathbf{b}_q \qquad (8)$$

with

$$\mathbf{B}_q = \mathbf{J}_q^T\mathbf{W}_d^T\mathbf{W}_d\mathbf{J}_q + \lambda\mathbf{C}_\mathbf{m}^{-1} \qquad (9)$$

and

$$\mathbf{b}_q = \mathbf{J}_q^T\mathbf{W}_d^T\mathbf{W}_d(\mathbf{d}-\mathbf{f}(\mathbf{m}_q)) - \lambda\mathbf{C}_\mathbf{m}^{-1}(\mathbf{m}_q-\mathbf{m}_0) \qquad (10)$$

where $\mathbf{J}_q$ is the Jacobian at iteration q and T denotes the transpose operator. For more details on the implementation of the inversion scheme, we refer to Kemna (2000) and Martin et al. (2010).

At each iteration, the regularization parameter is optimized in order to decrease the RMS (root-mean square) of error weighted data misfit according to the discrepancy principle (Hansen, 1998). The optimization process ends when the RMS of the data misfit reaches 1 (i.e. the data set is fitted within its error level assessed with reciprocal measurements).

Variogram parameters are not directly imposed during the optimization process (Martin et al., 2010). This allows us to run the algorithm without imposing the horizontal range which is often difficult to obtain. Johnson et al. (2007) also defined a degree of certainty for their variogram model. However, we will see that, in this study, the uncertainty is such that the matching level would have been very low for the horizontal variogram. In addition, an error in the horizontal variogram is not a critical issue. Indeed, Hansen et al. (2005) found in their synthetic study using sequential simulations that if longer or shorter ranges were imposed in the inversion process, the ranges calculated on the solution tended to be closer to the true ones than to the imposed ones. Yeh and Liu (2000) also discussed that their geostatistical inverse method within the context of hydraulic tomography was not very sensitive to correlation lengths except for large uncertainty altering the direction of anisotropy. They relate this observation to the fact that correlation length provides an estimate of the average size of heterogeneity. Its impact diminishes when more measurements are available. We observed a similar behavior in the inversion of our field data (see section 5.2). We thus deliberately introduced an erroneous horizontal range.

The inversion grid was built in order to have two elements between electrodes. The mean thickness of each grid cells was around 1m. Small variations occur due to the topography. Considering this grid cell size for ERT inversion, we assume that there are not significant

support effects on the variogram between EM39 conductivity measurements and ERT conductivity estimates. Indeed, according to McNeill (1986) the volume investigated by one EM39 measurements is quite similar to the grid cell size used here.

4.3. Image appraisal

Assessing the quality of an ERT image and the reconstruction of electrical resistivity/conductivity is a major issue when interpreting imaging results. In the following, we use the data error-weighted cumulative sensitivity as an image appraisal tool (e.g. Cassiani et al., 1998; Nguyen et al., 2009; Henderson et al., 2010). In accordance to Kemna (2000), we define the coverage or cumulative sensitivity (hereafter we will refer to it simply as the sensitivity) **S** as

$$\mathbf{S} = \mathrm{diag}\left\{\mathbf{J}^{\mathrm{T}}\mathbf{W}_{\mathrm{d}}^{\mathrm{T}}\mathbf{W}_{\mathrm{d}}\mathbf{J}\right\}, \qquad (11)$$

which depends on both data weighting and parameters. A high sensitivity value signifies that a change of this parameter is going to influence the predicted data strongly whereas a low value denotes less or no influence of this parameter on the predicted data. Obviously, a poorly covered region is unlikely to be well resolved and thus, the sensitivity may give some crude indication for how well the model parameter is represented by the data set. However, it must be emphasized, that high sensitivity does not necessary imply high resolution but rather represents a favoring factor.

The sensitivity as image appraisal tool can be used to define a cut-off value below which the results cannot be interpreted (e.g., Robert et al., 2011). This defines some kind of weighting/filtering scheme for the interpretation. The biggest difficulty, however, is to define this value. In this study, as borehole data is available, it is possible to compare calculated and measured values in order to choose an appropriate sensitivity threshold.

5. ERT imaging results

5.1. Investigation of prior models

From a statistical point of view, the prior model $\mathbf{m_0}$ (equation 7) equals the mean of the probability density function (Tarantola, 1987). If we assume that the random field of log electrical conductivity $Z(x)$ is stationary, the expectation $E(Z(x))$ is independent of x and the prior model is homogeneous. However, one may also guide the solution by choosing an appropriate prior model that honors the spatial distribution of the investigated parameters, i.e. spatial statistics and conductivity measurements in boreholes. A possibility here is to use a conditioned sequential Gaussian simulation (Deutsch and Journel, 1998) based on borehole data as a reference model.

An example is given in FIG. 6b where the solution is computed from equation 7 using the prior $\mathbf{m_0}$ shown in FIG. 6a, built with the variogram model (equation 4) described in section 4.1 and using the histogram of EM39 measurements as a targeted probability distribution. This figure corresponds to profile 3 (FIG.1B) with P14 measurements located in the middle of the section used as conditioning data.

Close to the surface, the inverted solution differs significantly from the prior and reflects the conductivity as forced by the data. In depth, where the sensitivity is low (for more details see section 5.4.1.), the solution reflects the prior model and shows large variations (resistivity higher than 1000 Ωm in saturated sand on the bottom left side whereas it is 100 Ωm in the well). In low sensitivity zones, parameter changes have almost no effect on the data misfit, and mainly contribute to the objective function through the model misfit. The latter decreases as the inverted model gets closer to the prior model.

Since the prior is only one possible realization, it is more meaningful to examine the mean of 50 inversions carried out with different realizations as prior model. The obtained solution (FIG. 6c) is now smoothed in depth and the conductivity values are close to the mean value of the conductivity distribution. This solution is close to the solution obtained with a

homogeneous prior model (FIG. 6d), in this case equal to 100 Ωm (this value was chosen according to EM39 measurements below –10 mTAW).

FIG. 6c suggests that salt water is found in two different separated zones. This is quite unlikely to occur in reality according to groundwater movement and results from the sequential Gaussian simulation used as a reference model, where the horizontal range plays an important role. Therefore, if the range is poorly estimated to deduce a good reference model, an implausible solution, with respect to the known hydrodynamics of the system, could result in terms of the salt water distribution. So, if the horizontal range seems to have a limited effect on the inversion through the covariance matrix, its effect is more important if Gaussian simulations are used to include prior conductivity information.

Given these results and to avoid an important effect of the unknown horizontal range on our solutions, we decided to use a homogeneous prior model based on EM39 measurements (below –10 mTAW, where the sensitivity is low) to invert the data for each profile. Doing so, we avoid a bias on the horizontal range due to the prior model and we impose a reasonable prior at depth.

5.2. Investigation of the role of the ranges

To illustrate the effects of the horizontal and vertical ranges on the inversion results, we provide a comparison of solutions obtained with selected horizontal and vertical ranges.

As discussed in section 4.2., previous works (e.g. Yeh and Liu, 2000) indicated that an error in the input ranges could be overcome by the information brought by the data. In this section, we compare inversion results obtained for Profile 1 (FIG. 8b) with ranges discussed in section 4.1. and two others inversions obtained with the horizontal ranges multiplied by 2 (FIG. 7a) and the vertical ranges multiplied by 2 (FIG. 7b), respectively.

From FIG. 7a and 8b, we see that multiplying the horizontal range by 2 does not change the solution drastically. The distribution of salt water is similar vertically; horizontally, it

appears to be slightly smoother, which is expected given the greater range. Even if we cannot compare the results with the true distribution, we see that when a greater range is used as input horizontal ranges, the distribution of conductivity is not highly different to the one obtained with the smaller range (e.g. the one determined with the anisotropy ratio of 4).

The vertical range appears to be a much more critical parameter. From FIG. 7b and 8b, we see that when using a greater range, we tend to recover a conductivity zone spread over a greater thickness with less contrast between salt and fresh water. This can be easily observed when the distributions are compared at a depth of −10 mTAW or when we look at the conductive zone at abscissae 50 m. The vertical correlation length given in the inversion through the covariance matrix will influence the vertical distribution of conductivity. In the example provided by FIG. 7b and 8b, it results in a smoother conductivity distribution.

5.3. Smoothness-constrained solution

For all profiles, a smoothness-constrained inversion (first order smoothing operator, see Kemna (2000)) was carried out in order to have reference estimates for comparison and to provide the solution that would be obtained if the prior knowledge about the conductivity distribution was not included in the inversion process as it is done in most studies. For the regularization, a horizontal to vertical smoothness ratio of 4 was used, which was the same for geostatistical regularization (see section 4.1.). All inversions were carried out with a data error estimate determined as outlined in section 3.2.2. In the following we confine the details of discussion to the results of Profile 1. Similar results were obtained for other profiles, too.

FIG. 8a shows the ERT results obtained with the standard smoothness-constraint regularization. The most expected feature can be identified as a conductive layer from 0 to –12 mTAW. As discussed previously, the increase in conductivity is mostly related to an increase in salt water content. However, the comparison with EM39 measurements in P11 and P12 (Fig. 9 a and b) highlights the fact that conductivity values remain too low in the area of

salt water (around 100 mS/m instead of 300 mS/m), whereas they are much higher than EM39 measurements below –10 mTAW (40 mS/m instead of 10 mS/m). Clearly, the contrast between sand filled with fresh and salt water is partly erased by the smoothness regularization. The obtained image is useful for a first qualitative interpretation, but there is a clear need to improve the solution to provide a quantitative interpretation.

5.4. Geostatistically constrained solution

The solution obtained with geostatistical regularization and a homogeneous prior model deduced from borehole data is presented in FIG. 8b. FIG. 9a and b validate the comparison of vertical conductivity profiles with EM39 data. Additionally, the latter figure also shows conductivity values for a solution where a sequential Gaussian simulation (computed on the basis of the EM39 data) was used as prior model. Hence, values for this solution are quantitatively closer to the EM39 data. However, elsewhere, the solution is similar to the one obtained with a homogeneous prior model, except at depth where the sensitivity is low and the prior model has most influence on the solution (see section 5.1).

The conductivity values in the fresh water of the aquifer are similar to the ones measured with the EM39 device (10 mS/m below –15 mTAW). Concerning the salt water infiltration, the conductivity values remain a little bit too low (200-250 mS/m), but the gap is small compared to the one observed for the smoothness-constrained solution. The thickness of the salt water lens is well recovered and a contrast is clearly visible between fresh and salt water (variations are sharper than for the smoothness-constrained solution). However, in some wells (P12 for example), the depth of the maximum conductivity value is not the same for ERT and EM39 data. This effect is likely due to the loss of sensitivity and resolution at depth and the difficulty to find a lower conductivity zone below salt water (current lines are focused in the high conductivity zone). In addition, since the vertical size of the grid cells is 1m, a better resolution cannot be expected. This improved solution relative to the smoothness-constrained

solution therefore allows a better qualitative (more details are visible) and quantitative (conductivity values are more realistic) interpretation.

FIG. 8b shows a shallow zone with high resistivity values (from about 500 Ωm up to more than 3000 Ωm), corresponding to the unsaturated dune sand close to the surface. The observed decrease in resistivity with depth (200-300 Ωm) corresponds to the saturated zone; the water level lies within 4 to 4.5 mTAW (Vandenbohede et al., 2008).

Another zone that appears clearly is the one located below −12 mTAW. Here, resistivity values are around 100 Ωm, ranging from 50 to 160 Ωm which corresponds well with the conductivity value for saturated sand of the dune aquifer above the clay of the Kortrijk formation.

Between these two zones, a conductive zone with resistivity values lower than 3 Ωm is present. This conductive region corresponds well to the salt water that infiltrated the pond. An interesting observation can be made on the left part of the section (from abscissa 0 to 40 m). Between −5 and −10 mTAW, a layer with resistivity values ranging from 15 to 30 Ωm can be found. These resistivity values are too low for sands with fresh water and too high for sands filled with salt water. Thus, we interpret it as the low permeability layer with more clay content. These findings are confirmed by the EM39 measurements, which were done before the salt water infiltration (FIG. 3A, thin dotted line) and also by the drilling logs (FIG. 3B). This layer, responsible for the lateral flow of salt water, is present in the complete section. Elsewhere, it is masked by the high conductivity values of the salt water, which makes it very difficult to discriminate clay and salt water content. However, in this particular zone, no salt water is present and thus it can be detected.

The intrusion itself can be correlated well to the high conductivity values which can be identified between 40 m and the end of the profile (FIG. 8). The maximum value of conductivity is located at a depth of –4 mTAW, above the clay layer. Around boreholes P11

and P12 (abscissa 60 m), the salt water appears slightly deeper along with the clay layer. This is confirmed by the EM39 measurements (FIG. 3A) where the clay is detected at −7 mTAW. This clay layer is therefore not a solid horizontal layer, but is laterally heterogeneous in thickness and may contain some discontinuities as well. Typically, such a clay layer is composed of several lenses, overlapping each other. This horizon is also quite local; indeed, it is not visible in FIG. 6d in the landward direction (left side of the figure). In consequence, salt water can also appear deeper down the aquifer. Since a hydraulic gradient exists from the dunes towards the sea, salt water circulation is possible below the semi-permeable layer.

High conductivity values are found near the surface around abscissa 70 m; this zone is too far from the entrance of the pond which makes a relation to a new infiltration unlikely. The EM39 logs (FIG. 3A) show a decrease in conductivity at 3 mTAW from 2005 to 2010. During the latter year, the presence of salt water is no longer detected in P11 at this depth and the conductive anomaly is attributed to a clay lens in the upper part of the Holocene deposits (see section 2.), acting also as a barrier to vertical flow. We can see from FIG. 8 that there may remain some salt water corresponding well with high conductivity values around abscissa 70 m on the top of these clay lenses; the inversion process tends to increase the conductivity value in the neighborhood of this location, because a correlation is assumed for cells located within a distance below the range. This could explain the difference between EM39 data and inversion results which are found in the near surface conductivity values displayed in FIG. 9b.

By computing the variograms (FIG. 10) of the inverted model shown in FIG. 8b, we obtain a vertical range very close to the one obtained from the borehole data (around 9 m); this observation shows the ability of the *a priori* model covariance matrix to impose the correct statistical characteristics vertically. As discussed in section 5.2., if another vertical range would be used, the resulting conductivity distribution would be different.

At the opposite, the horizontal range from the experimental variogram is very large (around 70 m) compared to the prior assumption (33.6 m), which further indicates the stratified nature of the area. We assume that the inversion could recover the horizontal range (which is unknown in our study case) if for a same depth, sensitivity is laterally constant. Thus, prior information would be less important in this direction than vertically, since the sensitivity decreases with depth. This hypothesis is supported by the results obtained by modifying the horizontal range (FIG. 7a).

The sill value is also slightly higher (around 0.5) than expected from borehole measurements (0.37, FIG. 5). A possible explanation is the low conductivity values observed close to the surface correlated with unsaturated sand of the dunes. The position of the boreholes is such that they are almost out of the zone of low conductivity, it is thus not significantly affecting the borehole data leading to a wider range of conductivity in ERT results, and consequently to higher variances.

FIG. 11 gives a pseudo 3D overview of the whole area showing the depth and lateral extension of the infiltration. In the north-eastern direction, salt water is found at least 50 m away from the boundary of the pond. In the south-western direction, the lateral extension is smaller, about 20 to 25 m. Landwards, the lateral flow is already indicated by EM39 measurements (Vandenbohede et al., 2008); ERT confirms this movement and shows that salt water is not very far from the wells where it was previously detected. According to our studies, salt water is present at 20-25 m away from the boundary of the infiltration pond, only ten meters further than the salt water measured in P14 and P16. ERT also provides new evidences for a lateral flow towards the sea, where no wells are available. Additionally, our results show that salt water does not globally reach the bottom part of the aquifer. However, due to the nature of this layer which may consist of overlapping clay lenses, salt water may

locally flow into deeper regions, explaining small contrasts in conductivity below –10 mTAW.

Two profiles stretched on the beach (profiles 2 and 5, northwestern direction) allow us to observe (FIG. 11) the salt water lens under the beach (drawn in FIG. 2, see section 2). We have to be careful when interpreting the dimensions of this salt water lens. The depth of the salt/fresh water transition is about –5 mTAW according to our results. In contrast, Lebbe (1999) found with borehole conductivity measurements a depth of about –10 mTAW. The difference results from the geostatistical regularization: we used variogram parameters coming from boreholes characteristic of the pond area; they are different from the ones corresponding to the beach area (the vertical correlation length is slightly higher) where the infiltration process of infiltration is different. The difference can be attributed to the non-stationarity of the electrical conductivity on this profile. If the vertical range of the beach area is used to invert the data, the salt water lens under the beach is better resolved in detriment of the pond area. Actually, the process is the same that what is observed in FIG. 7b. Nevertheless, our results are closer to the expected distribution than the smoothness-constrained solution (not shown here).

In FIG. 11, we can also observe the similarity between adjacent profiles. For example, profiles parallel to the sea display the same distribution of salt water. The conductivity values tend to decrease with increasing distance from the inlet entrance. Profile 4, located further away from the inlet entrance in the southeast direction, was set up among the dune area, outwards from the infiltration pond. The conductive region detected in the subsurface of this area (FIG. 11) indicates that a horizontal flow exists; the high conductivity values are mostly related to salt water where no infiltration can occur.

5.5. Assessment of imaging results

5.4.1 Image appraisal and cross validation

We compare inversion results and borehole data to derive a cut-off value for the sensitivity for P12 (FIG. 12), a similar behavior is observed for the other wells, too. First, we see that the sensitivity with depth behavior changes below the salt water intrusion. Indeed, below the depth of the maximum conductivity value, sensitivity decreases rapidly. This is plausible since current lines tend to flow through conductive bodies. From –10 mTAW and below, the sensitivity decreases asymptotically to low values reflecting poor resolution. The smoothness-constrained solution also shows that below –10 mTAW, the recovered conductivity values differ from the ones measured with the EM39 device.

For the geostatistical solution, the fit between EM39 measurements and inverted conductivity values is visually good down to –30 mTAW. A cut-off value as defined above would indicate where the inversion is controlled by the regularization rather than the data.

Another way to assess the validity of ERT is to compare the results obtained separately at the same location for different profiles. TABLE 1 summarizes the results of the 9 intersections. It is based on a qualitative appreciation of the misfit based on a visual comparison of the results.

On the whole, the results are satisfying. Obviously, there are some differences when the results are obtained from different profiles, the maximum conductivity value or its depth is sometimes a little bit different. The maximum conductivity values are quite different in the intersections between profiles 1 and 2 or profiles 1 and 3. Elsewhere, the results are similar. The depth of maximum conductivity is mostly the same, except in P14 (intersection of profiles 3 and 4).

5.4.2 Inference of total dissolved solid content

Previous sections indicate that ERT results are reliable enough to carry out a more quantitative interpretation. Several phenomena can be responsible for an increase in electrical conductivity. In this study, the two main reasons are the salt content and the clay content.

Unfortunately, it is impossible with only resistance measurements to discriminate the two (induced polarization measurements were also taken on the field but did not yield good results due to the diminishing effect of salinity on the electrochemical polarization mechanisms). Since clay acts as a barrier for salt water, the two low resistive bodies are overlapping. When the clay content is higher, the formation factor is also likely different and surface electrical conductivity plays a greater role. However, it is still interesting to transform resistivity into salinity to provide quantitative information on the monitoring of the artificial salt water intrusion. According to Van Meire and Lebbe (2003), the bulk conductivity of the sediments σ_b (in mS/m) is related to the total dissolved solid (*TDS*) content (in mg/l) by

$$TDS = 10F\sigma_b \ , \qquad (12)$$

where F is the formation factor of Archie's law (Archie, 1942). In agreement with Lebbe (1978), a homogeneous value of 3 was chosen for the formation factor. Using equation 12, it was possible to produce a *TDS* content map in the pond. According to EM39 measurements, conductivity values below 20 mS/m can be considered as sand filled with fresh water. Therefore, this value was chosen as a cut-off value to interpret conductivity in terms of salinity (above this value, the water is supposed to be fresh). Obviously, considering the assumptions above, the derived TDS values give just a rough estimate highlighting trends in salt water distribution.

FIG. 13 displays two different models deduced from the smoothness-constrained solution (13a) and the geostatistically constrained solution (13b). The same features can be observed as in FIG. 8. With the smoothness-constrained solution, the low resistive anomaly is flattened and thicker, leading to low TDS content (maximum value around 17,000 mg/l) in a larger volume, whereas the TDS image of the second solution (FIG. 13b) describes the true situation more likely. The maximum TDS content value (26,900 mg/l) is detected above the semi-permeable layer. The North Sea has a salt content of about 27,000 mg/l. Thus, the salt

concentration is still close to the one of the sea water in the center of the lens, whereas it is smaller at its outer border where the salt water is "older" and more diluted. We see that the intrusion is not continuous, but several plumes are observed. A possible explanation is the dynamic nature of the intrusion. In the beginning, sea entered the pond quite often during high tides, but the inlets are silting up and the frequency of intrusion decreases (Vandenbohede et al., 2008). The intrusion scheme is not continuous but episodic, what is reflected in the intrusion shape.

6. **Discussion**

The methodology that we followed can be applied if borehole data describing the parameter of interest (i.e. electrical conductivity or resistivity in our case) is available. However, if we want to use the geostatistical regularization, we have to check the validity of assumption of stationarity. It is the responsibility of the operator to decide if this hypothesis is reasonable or not. In the present case, this assumption is not too strong, because we are in a relatively homogeneous sand area with variable clay content. Moreover, microscopic heterogeneity can be considered constant on a macroscopic scale, which would imply weak stationarity.

In our study, a stationarity issue appears when the electrical resistivity tomography profile crosses two different geological environments. Profile 2, for example, begins in the dune area but ends on the beach where salt water is found just below the surface (see FIG. 11). In these two environments, variogram parameters are different and it is not correct to apply the same value on the whole section (the assumption of stationarity is violated). However, it is also difficult to deterministically place a limit between these two environments and to invert them separately (i.e. each zone with its own variogram and without correlation between the zones) because points close to each other could have completely different conductivity values when they are close to this limit. Such an inversion would result in a

better description of the salt water distribution on the whole section, but would present a discontinuity.

In some geological environments, the use of a two-point correlation method (based on the variogram) could lead to unrealistic results. Indeed, these methods are able to describe smoothly heterogeneous media but inadequate when facing complex structures (Strebelle et al., 2002) such as multimodal distributions, with interconnected and curvilinear structures, those of alluvial plains or turbiditic reservoirs for example. To overcome these limitations, multiple-point statistics can be used. All these techniques are based on a training image. Its role is to depict the conceptual geological patterns of the site (Guardiano and Srivatsava, 1993). In more complex geological environments, it could thus be necessary to use another technique to correlate neighbor cells. However, even when the assumption of stationarity is violated, we showed that the geostatistical regularization provides results at least as good as the smoothness-constrained solution.

Another important point is the choice of the prior model. In our case, it seems pointless to use 50 simulations to obtain an image similar to the one obtained with a single inversion. However, different realizations can be useful to provide several scenarios of contamination in a stochastic approach. This approach can only be used when the horizontal range is known well enough, because it has a significant influence on the effect of borehole data around wells. In addition, in our studies, the number of boreholes was limited and conditioned Gaussian simulation let a lot of unconditioned zones influencing the inverse solution, limiting the advantage of including borehole data in the inverse problem. It could be more effective to impose borehole data by a different way, for example using an additional term in the objective function (equation 6) taking care of the misfit between model estimates and the (exact) measured parameters.

As illustrated by the results, the methodology developed here has several advantages compared to the standard smoothness-constrained inversion. Our solution using geostatistical regularization relies on a regularization operator deduced from borehole data (thus hard data). Here, the hypothesis made on the model roughness seems less strong than in the smoothness-constrained solution, since the correlation length is based on borehole conductivity measurements. It does not mean that the smoothness-constrained solution should be always rejected, since it can provide good estimates of conductivity distribution in a broad range of applications. Our approach is also more general than inversions imposing measured parameters at borehole locations. Indeed, prior information is spread all over the image plane through the inversion scheme. The misfit in boreholes was highly improved and the benefit remained likely true elsewhere in the section. Doing so, we increased our knowledge of the investigated groundwater reservoir with a realistic model of salt water distribution, which could be used for further studies in the Westhoek area.

7. **Conclusion**

Spatial covariance estimates derived from borehole data were used to constrain the inversion of surface ERT as formulated previously by several authors at a hydrogeologically relevant scale (hundreds of meters) in an innovative way using EM39 data. Variograms were computed to model borehole data which were then transformed and parameterized by an *a priori* model covariance matrix to regularize the inversion scheme. Inversions carried out with the data collected in the Westhoek nature reserve permitted to fully appreciate the improvement brought by the model covariance matrix regularization. If smoothness-constrained solutions are useful in a broad range of applications and were sufficient for a qualitative interpretation, in this particular case, comparisons with EM39 measurements proved that the new type of regularization was able to give significantly better results, concerning conductivity values, shape and depth of the salt water intrusion. In addition, in our

specific field case, the scheme preserves the vertical spatial statistics. Inversions with model covariance matrix as a regularization tool were always better and enabled a quantitative interpretation of the imaging results. It is important to emphasize that prior information can be used to constrain the inversion in the whole image plane, and not only around boreholes as it is currently possible with commercial software. We think that the methodology described in this paper could apply to other contexts, where geostatistical information is available

The sensitivity based threshold, used for image appraisal, indicates where the inversion is less controlled by the data. A reasonable prior model can therefore help to increase imaging quality with depth, for less covered areas. This further emphasizes the importance of the prior model.

The survey performed on the site of "the Westhoek", based mainly on electrical resistivity tomography and EM39 measurements, was able to provide a coherent image for the state of water salinity due to the artificial infiltration in the eastern inlet. Six profiles (3 parallel and 3 perpendicular to the coast line) allowed getting a detailed description of the intrusion in three dimensions. The depth (around – 4 mTAW, limited by the clayey layer) and the lateral extensions (more than 50 m in the northeastern direction, 25 m landward) were determined thanks to profiles going further away from the pond than boreholes placed on the perimeter. ERT also gave evidence for a lateral flow towards the sea, where no well is drilled. The distribution of TDS content along the profiles showed the complexity of the intrusion shape due to an episodic infiltration scheme.

The results obtained for the Westhoek site emphasize the need to go beyond standard smoothness-constrained inversion when it fails to reproduce expected structure and to use available borehole data as prior information to constrain the inversion.

Acknowledgments

AVDB is supported by the Fund for Scientific Research — Flanders (Belgium) where he is currently a postdoctoral fellow. TH is supported by the F.R.S.-FNRS as PhD student fellow. EM39 measurements were done for the monitoring program by order of the Ministry of Transport and Public Works, Agency for Maritime and Coastal Services, Coastal Division. This ministry and the Agency of Nature and Forestry are thanked for granting permission to do the necessary field work. We would like to thank four anonymous reviewers for their constructive remarks leading to a great improvement of the manuscript.

References

Amidu, S.A., Dunbar, J.A., 2008. An evaluation of the electrical-resistivity method for water-reservoir salinity studies. Geophysics, 73 (4), G39-G49. doi: 10.1190/1.2938994.

Archie, G.E., 1942. The electrical resistivity log as an aid in determining some reservoir characteristics. Transactions AIME, 146, 54-62.

Carter, E.S., White, S.M., Wilson, A.M., 2008. Variation in groundwater salinity in a tidal salt marsh basin, North Inlet Estuary, South Carolina. Estuarine, coastal and shelf science, 76, 543-552. doi: 10.1016/j.ecss.2007.07.049.

Cassiani, G., Böhm, G., Vesnaver, A., Nicolich, R., 1998. A Geostatistical Framework for Incorporating Seismic Tomography Auxiliary Data into Hydraulic Conductivity estimation, Journal of Hydrology, 29(1-2), 58-74.

Chasseriau, P., Chouteau, M., 2003. 3D gravity inversion using a model of parameter covariance. Journal of applied geophysics, 52, 59-74.

Constable, S.C., Parker, R.L., Constable, C.G., 1987. Occam's inversion: a practical algorithm for generating smooth models from electromagnetic sounding data. Geophysics, 52 (3), 289-300.

Dahlin, T., Zhou, B., 2004. A numerical comparison of 2D resistivity imaging with ten electrode arrays. Geophysical prospecting, 52, 379-398. doi: 10.1111/gpr.2004.52.issue-5.

Day-Lewis, F.D., Lane Jr., J.W. 2004. Assessing the resolution-dependent utility of tomograms for geostatistics. Geophysical research letters, 31, L07503, doi:10.1029/2004GL019617.

De Franco, R., Biella, G., Tosi, L., Teatini, P., Lozej, A., Chiozzotto, B., Giada, M., Rizzetto, F., Claude, C., Mayer, A., Bassan V., Gasparetto-Stori, G., 2009. Monitoring the saltwater intrusion by time lapse electrical resistivity tomography: The Chioggia test site (Venice

Lagoon, Italy). Journal of applied geophysics, 69, 117-130. doi: 10.1016/j.jappgeo.2009.08.004.

deGroot-Hedlin, C., Constable, S., 1990. Occam's inversion to generate smooth, two dimensional models from magnetotelluric data. Geophysics, 55, 1613-1624.

Deutsch, C.V., Journel, A.G., 1998. GSLIB : geostatistical software library: and user's guide, second edition, Oxford University Press, New York, NY, 369 pp.

Goldman, M., Kafri, U., 2006. Hydrogeophysical applications in coastal aquifers, in: Vereecken, H., Binley, A., Cassiani, G., Revil, A., Titov, K. (Eds.), Applied hydrogeophysics. Nato Science Series, Serie IV, Earth and environmental sciences, 71, Springer, Dordrecht, 233-254.

Guardiano, F.B., Srivatsava, R.M., 1993. Multivariate geostatistics: beyond bivariate moments, in: Geostatistics Troia '92, Soares, A. (Eds.), Kluver Academic Publishers, Dordrecht, 133-144.

Hansen, P. C., 1998. Rank-deficient and discrete ill-posed problems: numerical aspects of linear inversion. SIAM, Philadelphia.

Hansen, T.M., Journel, A.G., Tarantola, A., Mosegaard, K., 2006. Linear inverse Gaussian theory and geostatistics. Geophysics, 71 (6), R101-R111.

Henderson, R.D., Day-Lewis, F.D., Abarca, E., Harvey, C.F., Karam, H.N., Liu, L., Lane, J.W. Jr., 2010, Marine electrical resistivity imaging of submarine groundwater discharge: sensitivity analysis and application in Waquoit Bay, Massachussets, USA.

Isaaks, E.H., Srivastava, R.M., 1989. Applied geostatistics, Oxford University Press, New-York, 561pp.

Johnson, T.C., Routh, P.S., Clemo, T., Barrash, W., Clement, W.P., 2007. Incorporating geostatistical constraints in nonlinear inversion problems. Water resources research, 43, W10422, doi:10.1029/2006WR005185.

Journel, A.G., Huijbregts, C.J., 1978. Mining geostatistics, Academic Press, London, New York.

Kemna, A., 2000. Tomographic inversion of complex resistivity – theory and application, PhD thesis, Ruhr-University of Bochum.

LaBrecque, D.J., Miletto, M., Daily, W., Ramirez, A., Owen, E., 1996. The effects of noise on Occam's inversion of resistivity tomography data. Geophysics, 61 (2), 538-548.

Lebbe, L., 1978. Hydrogeologie van het duingebied ten westen van De Panne, PhD Thesis, University of Ghent, Ghent, 164pp, unpublished.

Lebbe, L., 1999. Parameter identification in fresh-saltwater flow based on borehole resistivities and freshwater head data. Advances in water resources, 22 (8), 791-806.

Linde, N., Binley, A., Tryggvason, A., Petersen, L.B., Revil, A., 2006. Improved hydrogeophysical characterization using joint inversion of cross-hole electrical resistance and ground-penetrating radar traveltime data. Water Resource Research, 42, W12404, doi: 10.1029/2006WR005131.

Martin, R., Kemna, A., Hermans, T., Nguyen, F., Vandenbohede, A., Lebbe, L., 2010. Using geostatistical constraints in electrical imaging for improved reservoir characterization, Abstract H23L-06 presented at 2010 Fall Meeting, AGU, San Francisco, Calif., 13-17 Dec.

Martínez, J., Benavente, J., García-Aróstegui, J.L., Hidalgo, M.C., Rey, J., 2009. Contribution of electrical resistivity tomography to the study of detrital aquifers affected by seawater intrusion-extrusion effects: The river Vélez delta (Vélez-Málaga, southern Spain). Engineering geology, 108, 161-168.

Maurer, H., Holliger, K., Boerner, D.E., 1998. Stochastic regularization : smoothness or similarity? Geophysical research letters, 25, 2889-2892.

McNeill, J.D., 1986. Geonics EM39 borehole conductivity meter - Theory of operation, Geonics Limited technical note TN-20.

Nguyen F., Kemna, A., Antonsson, A., Engesgaard, P., Kuras, O., Ogilvy, R., Gisbert, J., Jorreto, S., Pulido-Bosch, A., 2009. Characterization of seawater intrusion using 2D electrical Imaging. Near surface geophysics, 7, 377-390. doi: 10.1007/s11119-009-9156-7.

Parasnis, D.S., 1988. Reciprocity theorems in geoelectric and geoelectromagnetic work. Geo-exploration, 25, 177-198.

Pilkington, MM, Todoeschuck, J.P., 1991. Naturally smooth inversion with a priori information from well logs. Geophysics, 56, 1811-1818.

Robert, T., Dassargues, A., Brouyère, S., Kaufmann, O., Hallet, V., Nguyen, F., 2011. Assessing the contribution of electrical resistivity tomography (ERT) and self-potential (SP) methods for a water well drilling program in fractured/karstified limestones, Journal of applied geophysics, 75, 42-53.

Slater, L., Binley, A.M., Daily, W., Johnson, R., 2000. Cross-hole electrical imaging of a controlled saline tracer injection. Journal of applied geophysics, 44, 85-102.

Smith, J.T., Booker, J.R., 1988. Magnetotelluric inversion for minimum structure. Geophysics, 53, 1565-1576.

Strebelle, S., Payrazyan, K., Caers, J., 2002. Modeling of a deepwater turbidite reservoirs conditional to seismic data using multiple-point geostatistics, paper presented at SPE Annual Technical Conference and Exhibition, Society of Petroleum Engineers Inc, San Antonio, Texas.

Tarantola, A., Valette, B., 1982. Generalized non-linear problems solved using the least-squares criterion. Review of geophysics and space physics, 20, 219-232.

Tarantola, A., 1987. Inverse problem theory. Elsevier, Amsterdam.

The Earth Institute - Columbia University, 2006. It's 2025. Where do most people live? Columbia University, New-York. http://www.earth.columbia.edu/news/2006/story07-11-06.php

Tikhonov, A.N., Arsenin, V.A., 1977. Solution of ill-posed problems, Winston & Sons, Washington.

Vandenbohede, A., Lebbe, L., 2006. Occurrence of salt water above fresh water in dynamic equilibrium in coastal groundwater flow systems. Hydrogeology Journal, 14 (4), 462–472.

Vandenbohede, A., Lebbe, L., Gysens, S., Delecluyse, K., DeWolf, P., 2008. Salt water infiltration in two artificial sea inlets in the Belgian dune area. Journal of hydrology, 360, 77-86.

Van Meir, N., Lebbe, L., 2003. Deriving TDS values in coarse sediments from long normal and electromagnetic logs. Ground water, 41 (1), 33-40.

Verwaest, T., De Wolf, P., Herrier, J.-L., Leten, M., 2005. Windows in the dunes - the creation of sea inlets in the nature reserve de Westhoek in de Panne, in: Herrier, J.-L., Mees, J., Salman, A., Seys, J., Van Nieuwenhuyse, H., Dobbelare, I. (Eds.), Proceedings "Dunes end Estuaries 2005" - International Conference on Nature Restoration Practices in European Coastal Habitats, Koksijde, Belgium, 19-23 September 2005, vol. 19. VLIZ Special Publication, 433-439.

Yang, X., LaBrecque, D.J., 1998. Stochastic inversion of 3D ERT data. Symposium on the application of geophysics to engineering and environmental problems, EEGS, 11, 221-228.

Yeh, T.-C. J., Jin, M., Hanna, S., 1996. An iterative stochastic inverse method: conditional effective transmissivity and hydraulic head fields, Water resources research, 32(1), 85-92.

Yeh, T.-C. J., Liu, S., 2000. Hydraulic tomography: Development of a new aquifer test method, Water resources research, 36(8), 2095-2105.

Yeh, T.-C. J., Liu, S., Glass, R. J., Baker, K., Brainard, J.R., Alumbaugh, D., LaBrecque, D., 2002. A geostatistically based inverse model for electrical resistivity surveys and its applications to vadose zone hydrology, Water resource research, 38(12), doi:10.1029/2001WR001204.

Yeh, T.-C. J., Zhu, J., Englert, A., Guzman, A., Flaherty, S., 2006. A successive linear estimator for electrical resistivity tomography. Applied hydrogeophysics, edited by Vereecken, H., Binley, A., Cassiani, G., Revil, A., Titov, K. NATO Science Series, Springer, pp 383.

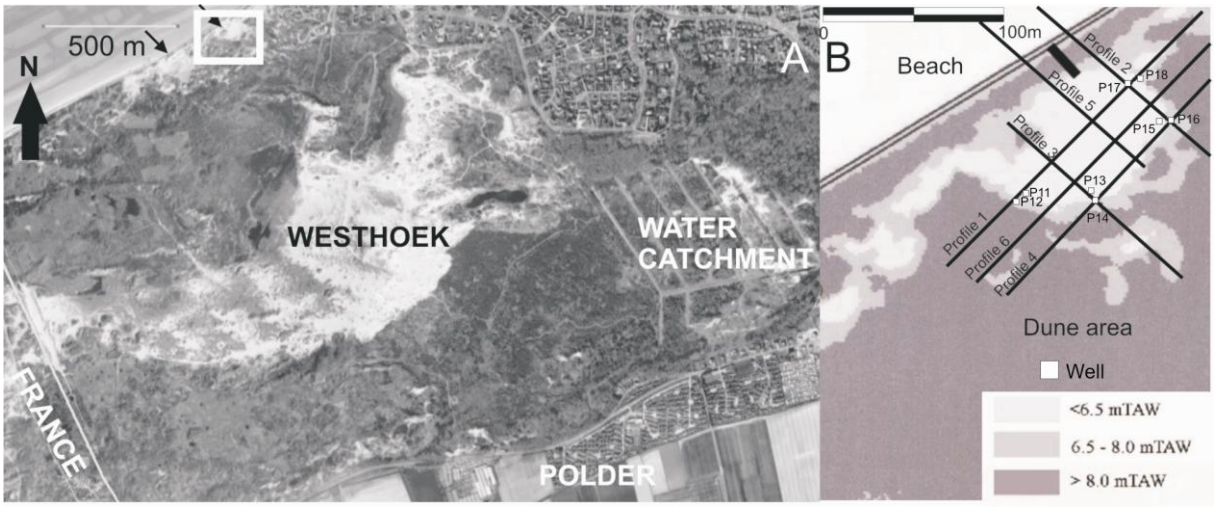

FIGURE 1 : Site Location. The site is located in the western Belgian coast plain (a), the two artificial sea inlets are indicated by black arrows, the white rectangle is zoomed in (b) which shows the location of the ERT profiles and the position of the wells in the eastern pond.

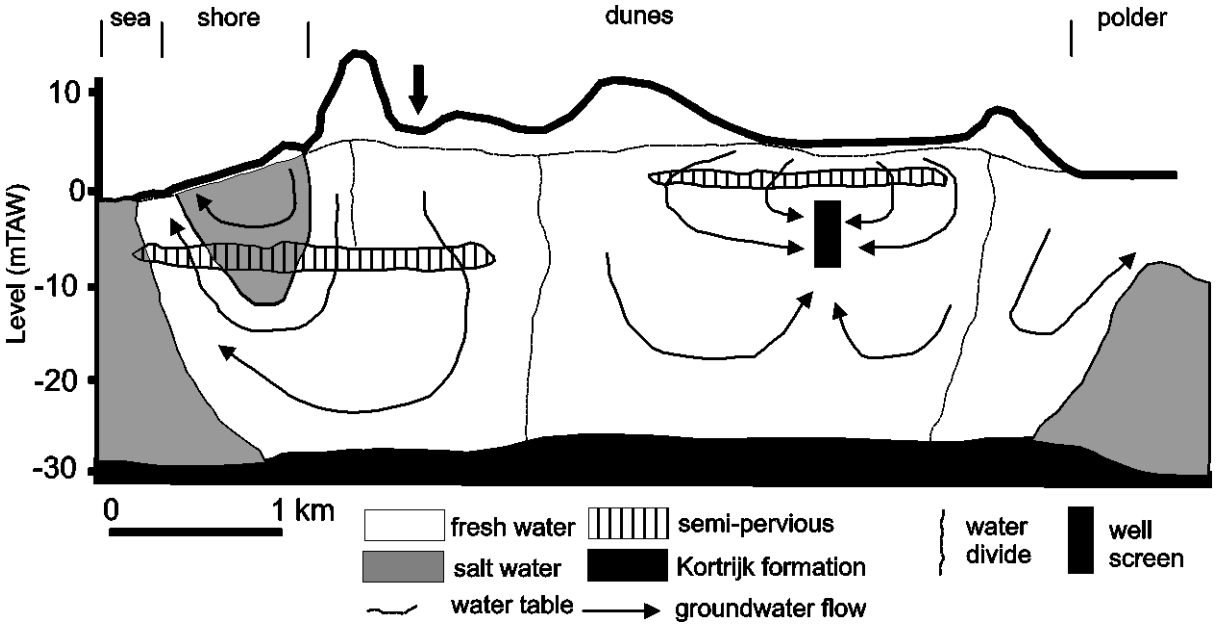

FIGURE 2 : Hydrogeology of the study site. This schematic cross-section describes the geology of the site, groundwater flows, the fresh/salt water distribution and the position of water divides before infiltration. The black arrow indicates the position of the inlets.

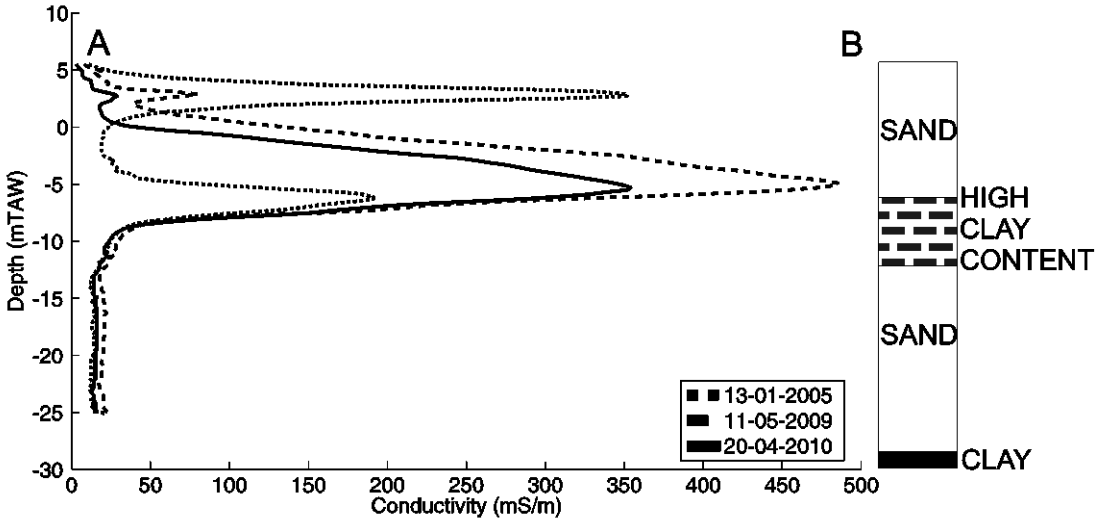

FIGURE 3 : EM39 measurements. EM39 measurements carried out in well P11 at different time between 2005 and 2010 shows an increase in electrical conductivity where salt water occurs (a), the position of the salt water is correlated with a high clay content layer highlighted by borehole logs (b)**.**

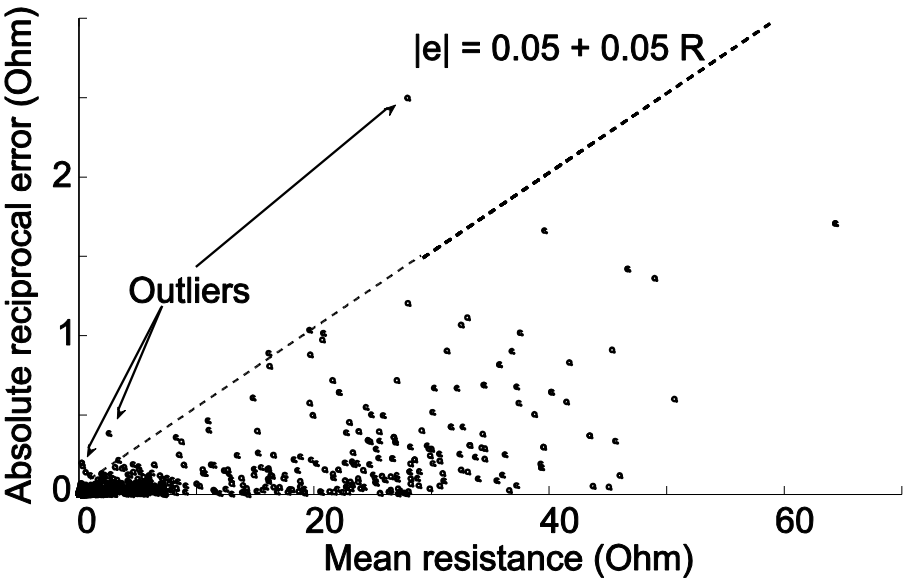

FIGURE 4 : Error assessment. Reciprocal resistance measurements were collected for every profile to assess the error level of the site. The dotted line shows the envelope of the absolute reciprocal error for the data set, it shows a linear trend with a minimum absolute error *a* equal to 0.05 Ω and a relative error *b* of 5%.

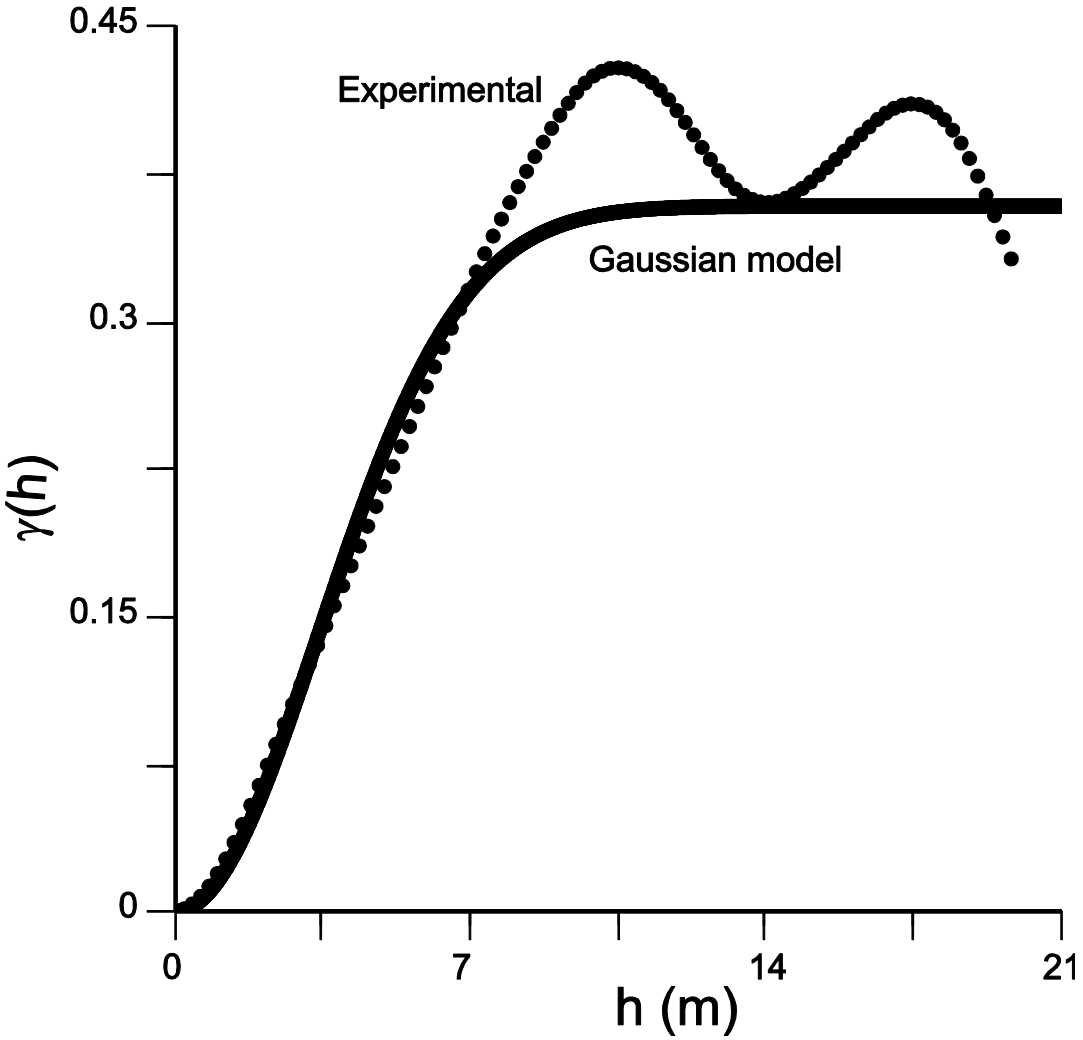

FIGURE 5 : Vertical variogram. The experimental vertical variogram of log electrical conductivity (points) was modeled (line) for the complete borehole data set with a Gaussian model. The sill value is equal to 0.37 and the range is equal to 8.4 m.

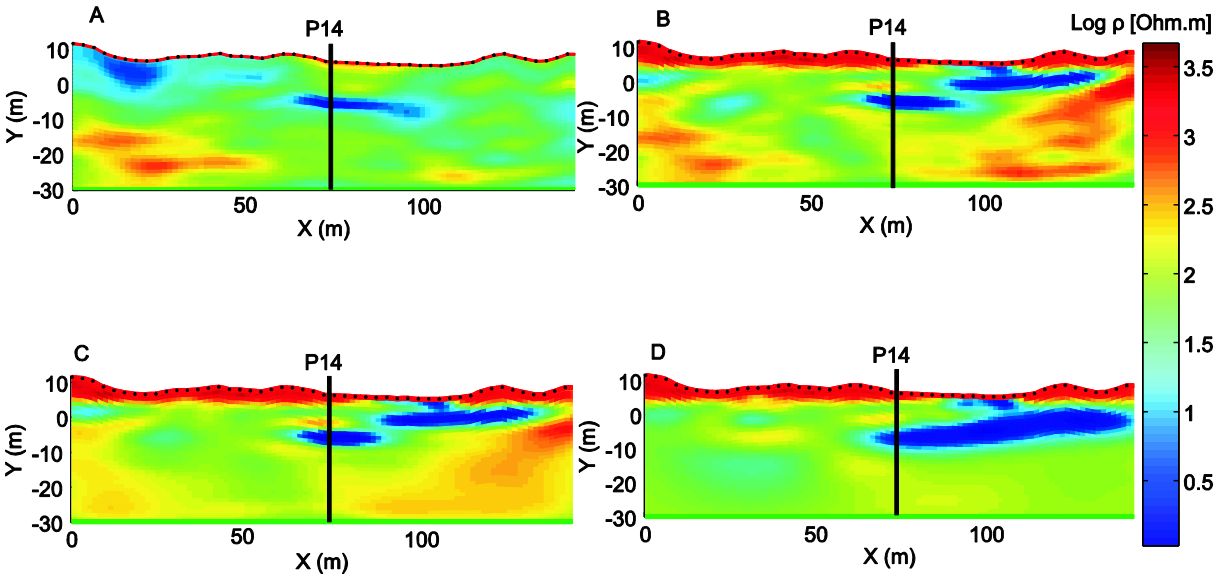

FIGURE 6 : Prior model. Several inversions were run with different prior models. (a) shows the prior model used to calculate (b), (c) is the mean calculated with 50 different inversions and (d) is the solution obtained with a homogeneous prior model.

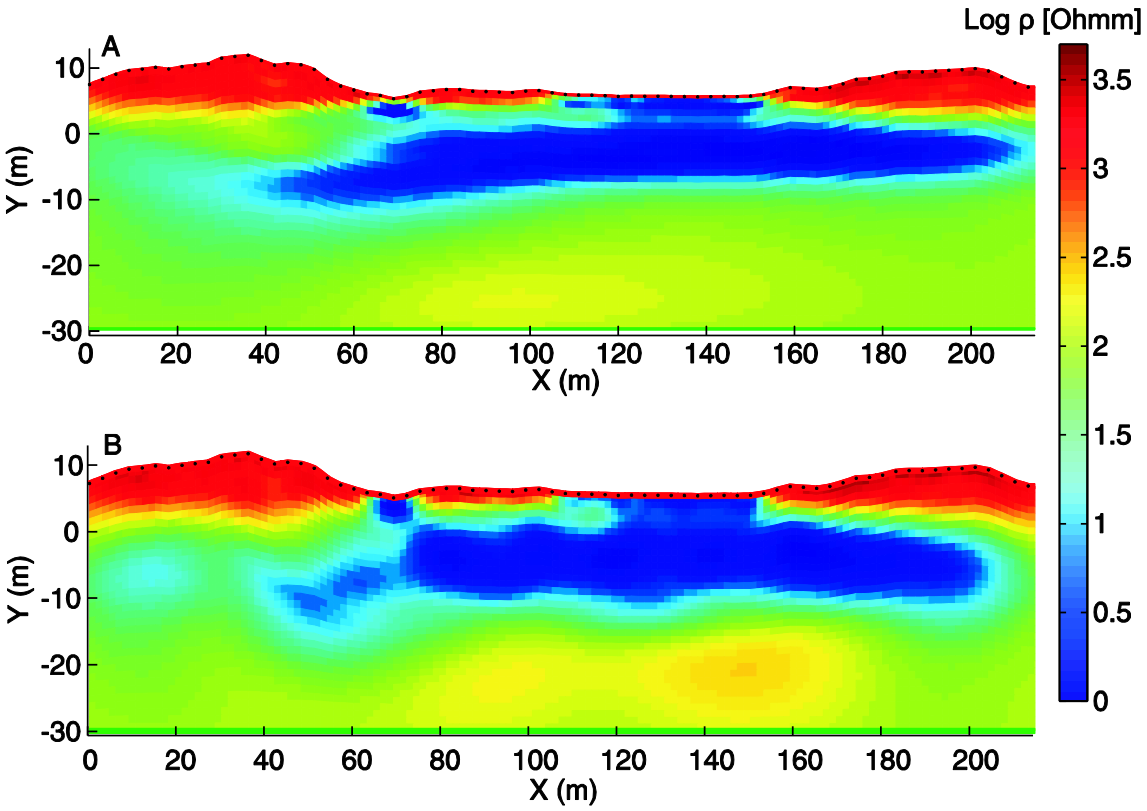

FIGURE 7 : Effect of the ranges on the inversion results. (a) The role of the horizontal range was highlighted by inverting the data with a range 2 times greater compared to FIGURE 8b showing few differences. (b) The role of the vertical range was highlighted by inverting the data with a range 2 times greater compared to FIGURE 8b showing a significant effect on the vertical distribution of conductivity.

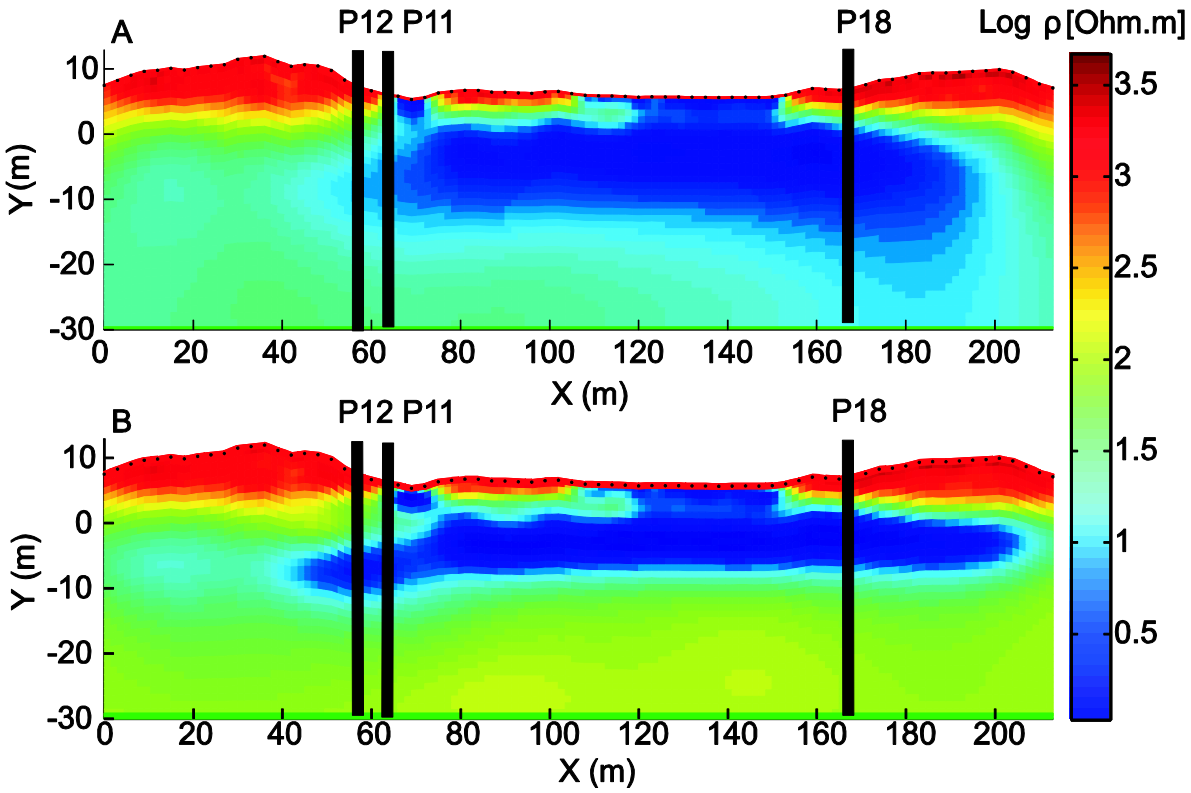

FIGURE 8 : Results for profile 1. The smoothness-constrained solution for profile 1 (a) provides poor results relative to the geostatistically constrained solution based on the variogram of FIGURE 4 (b). The latter shows sharper structure and resistivity values closer to the EM39 measurements. The three vertical black lines show the position of the wells P11, P12 and P18.

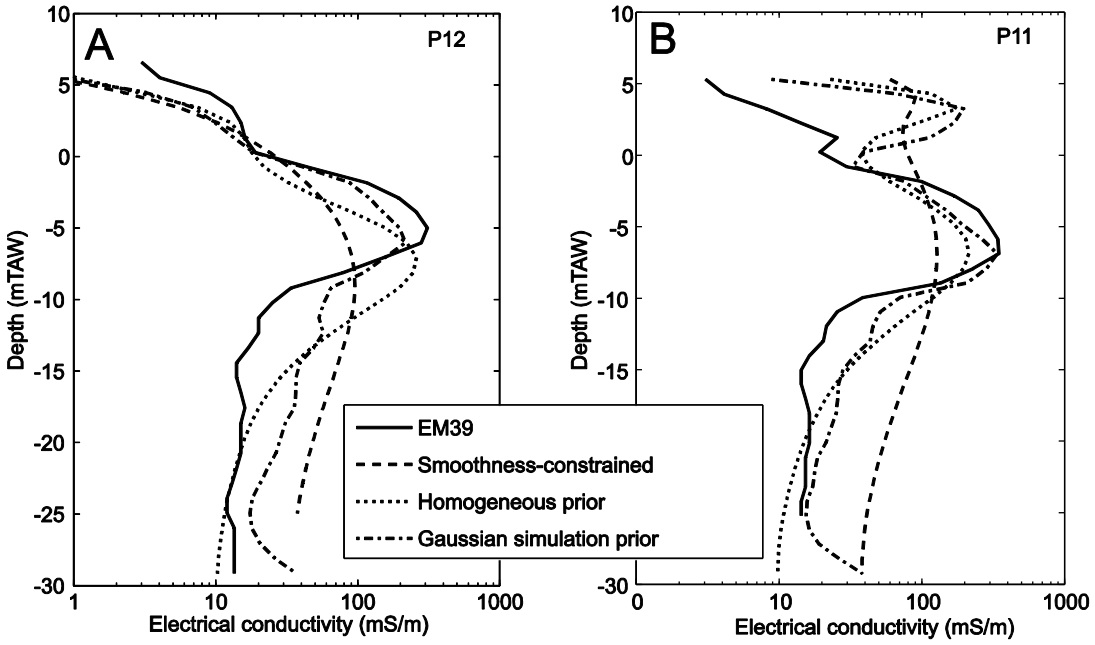

FIGURE 9 : Comparison with EM39 measurements. Borehole EM39 measurements (a) in well P12 (located at abscissa 57 m on the profile) and (b) in well P11 (located at abscissa 64 m on the profile) were used to assess the quality of different inversions. There is a clear improvement using the geostatistically constrained regularization against the smoothness constraint regularization.

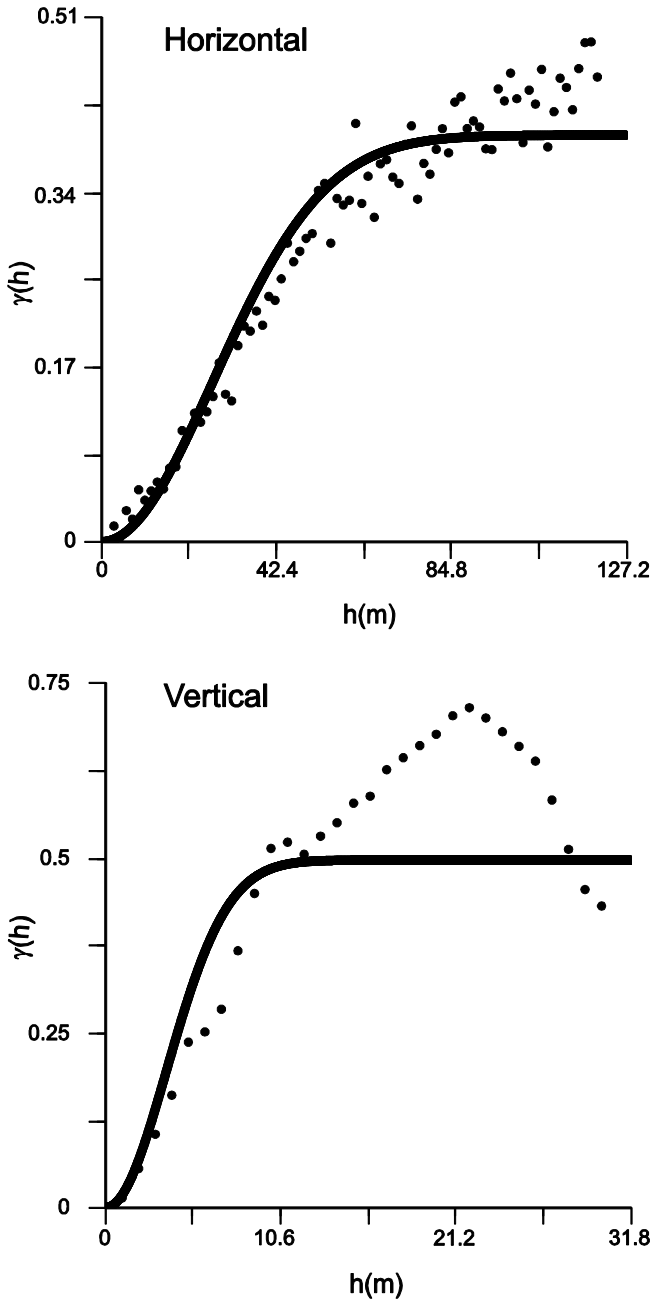

FIGURE 10 : Variogram after inversions. The vertical variogram calculated on the solution displayed in FIGURE 8b is close to imposed one with a range of 9 m. The horizontal range is much larger.

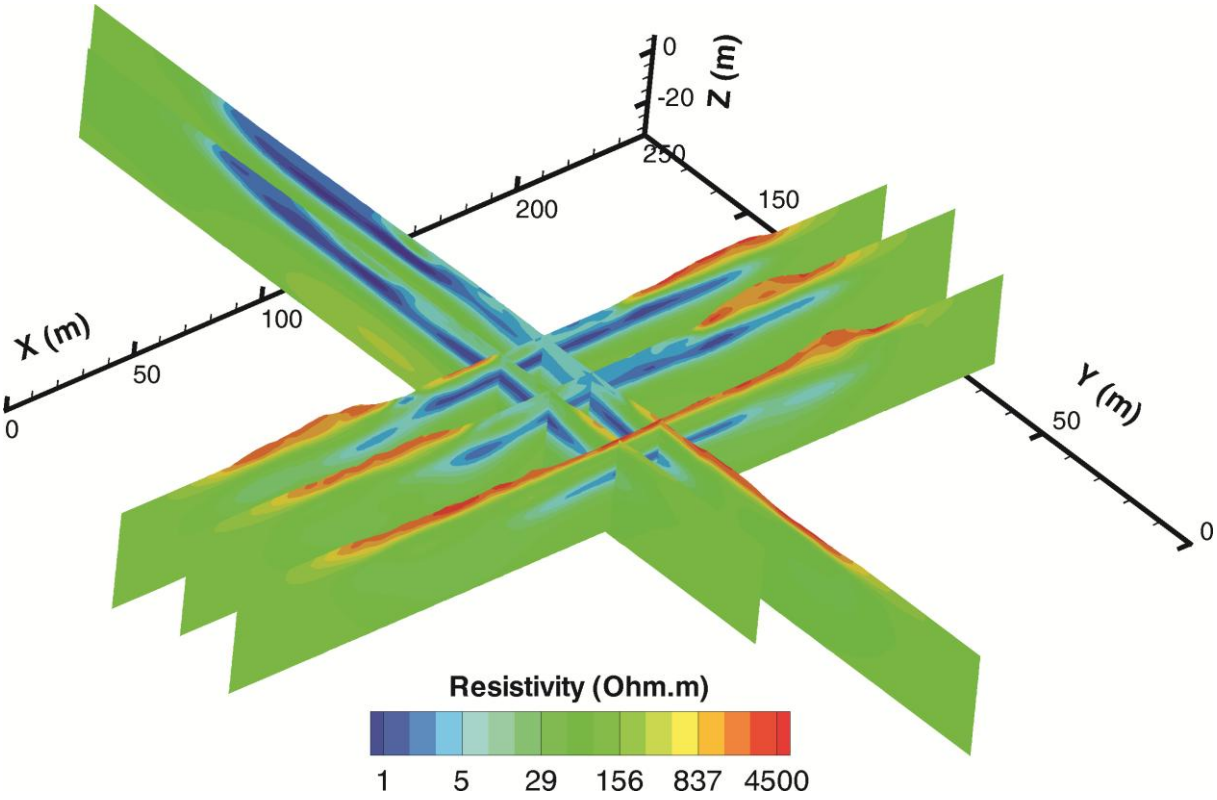

FIGURE 11 : Results for the entire site. The electrical resistivity distribution can be appreciated for all six profiles. The same features are visible as explained in FIGURES 8 and 9, the extensions of the plume are observable in all directions. The black arrow shows the limit between the infiltration pond and the beach.

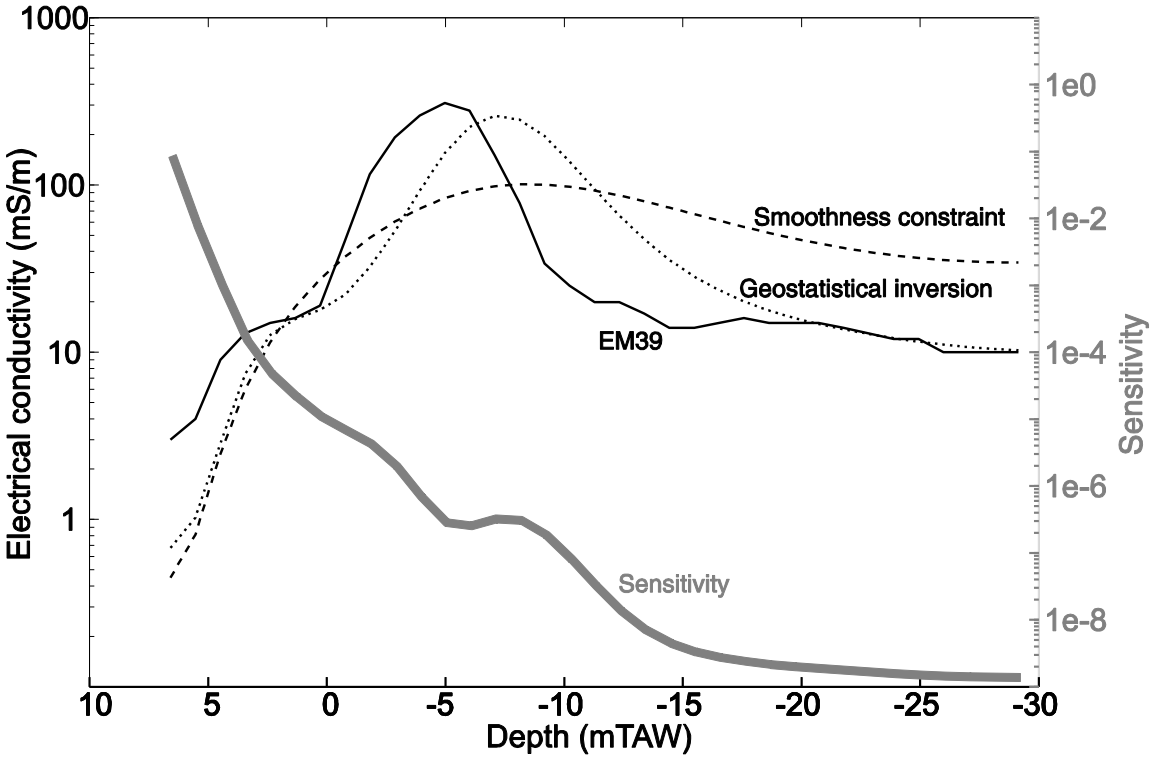

FIGURE 12 : Sensitivity analysis. The sensitivity was calculated to assess the quality of the inversions and was compared with borehole data. The left axis shows borehole data and inversion results, the right axis shows the value of sensitivity. A sill is observed in the sensitivity at the location of salt water. It may be used to define a cut-off value to interpret the data for the smoothness-constrained solution or to highlight where the solution is controlled by the regularization process for the geostatistically constrained solution.

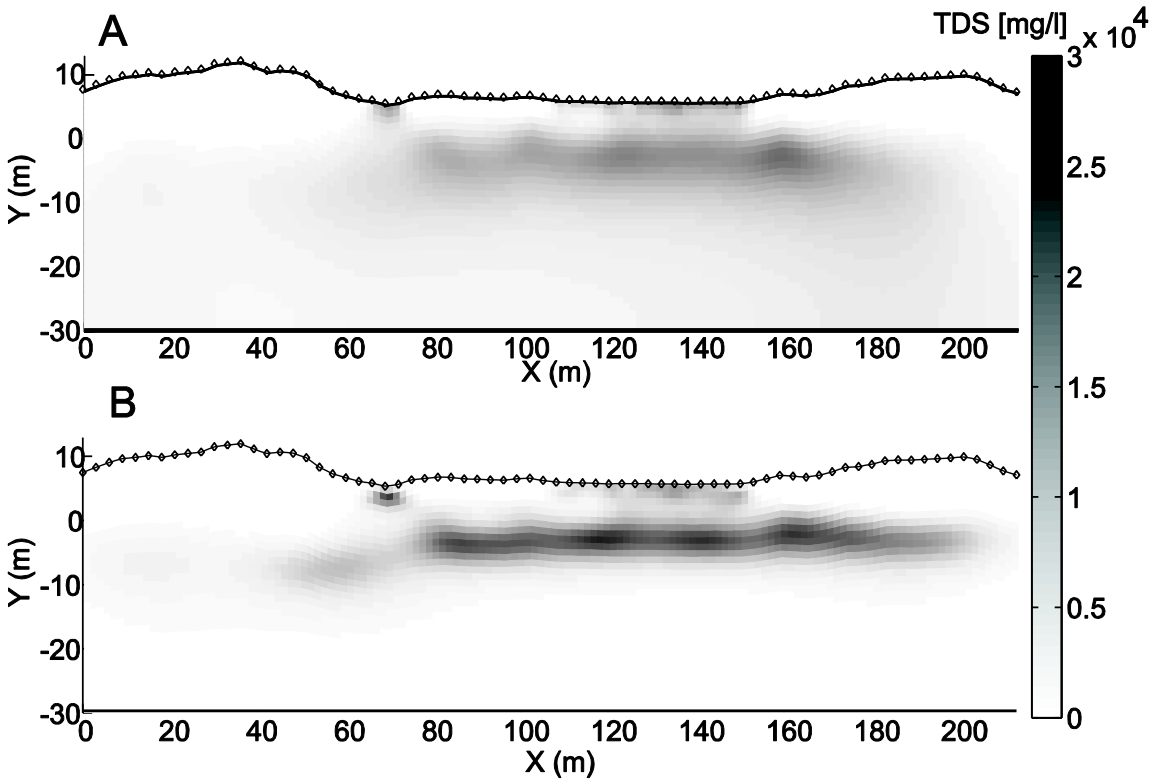

FIGURE 13 : TDS map. The TDS content was calculated from electrical resistivity for (a) the smoothness-constrained resistivity inverted model and (b) geostatistical regularized inverted model. For the latter, the maximum TDS content value is close to the one of the North Sea (27000 mg/l).

Couple of profiles	Abscissa of intersection (first profile) in m	Abscissa of intersection (second profile) in m	Quality of correlation	
			Depth of maximum	Value of maximum
P1 –P2	123	105	++	–
P1-P5	106.5	43.5	++	++
P1-P3	83	112.5	++	–
P6-P2	115.5	88.5	+	++
P6-P5	101	30	+	+
P6-P3	78	96	+	+
P4-P2	123	67	++	+
(P4-P5)	101.5	7	++	–
P4-P3	81	72	–	+

TABLE 1 : Cross-validation. The intersections between profiles (quality of the correlation : ++ = excellent, + = good, – = bad) were used to assess the quality of the inversion. Globally, the results are satisfying. The intersection between profiles 4 and 5 is not representative because it is located on the side of profile 5, where the sensitivity is low even close to the surface.